2017

Self-Assembly of Flexible Free-Standing 3D Porous MoS2-Reduced Graphene Oxide Structure for High-Performance Lithium-Ion Batteries

Yunfeng Chao
University of Wollongong, yc682@uowmail.edu.au

Rouhollah Jalili
University of Wollongong, rjalili@uow.edu.au

Yu Ge
University of Wollongong, yg711@uowmail.edu.au

Caiyun Wang
University of Wollongong, caiyun@uow.edu.au

Tian Zheng
University of Wollongong, tz648@uowmail.edu.au

See next page for additional authors

Publication Details

Chao, Y., Jalili, R., Ge, Y., Wang, C., Zheng, T., Shu, K. & Wallace, G. G. (2017). Self-Assembly of Flexible Free-Standing 3D Porous MoS2-Reduced Graphene Oxide Structure for High-Performance Lithium-Ion Batteries. Advanced Functional Materials, 27 (22), 1700234-1-1700234-10.

Self-Assembly of Flexible Free-Standing 3D Porous MoS2-Reduced Graphene Oxide Structure for High-Performance Lithium-Ion Batteries

Abstract

Flexible freestanding electrodes are highly desired to realize wearable/flexible batteries as required for the design and production of flexible electronic devices. Here, the excellent electrochemical performance and inherent flexibility of atomically thin 2D MoS2 along with the self-assembly properties of liquid crystalline graphene oxide (LCGO) dispersion are exploited to fabricate a porous anode for high-performance lithium ion batteries. Flexible, free-standing MoS2-reduced graphene oxide (MG) film with a 3D porous structure is fabricated via a facile spontaneous self-assembly process and subsequent freeze-drying. This is the first report of a one-pot self-assembly, gelation, and subsequent reduction of MoS2/LCGO composite to form a flexible, high performance electrode for charge storage. The gelation process occurs directly in the mixed dispersion of MoS2 and LCGO nanosheets at a low temperature (70 °C) and normal atmosphere (1 atm). The MG film with 75 wt% of MoS2 exhibits a high reversible capacity of 800 mAh g−1 at a current density of 100 mA g−1 . It also demonstrates excellent rate capability, and excellent cycling stability with no capacity drop over 500 charge/discharge cycles at a current density of 400 mA g−1 .

Disciplines

Engineering | Physical Sciences and Mathematics

Publication Details

Chao, Y., Jalili, R., Ge, Y., Wang, C., Zheng, T., Shu, K. & Wallace, G. G. (2017). Self-Assembly of Flexible Free-Standing 3D Porous MoS2-Reduced Graphene Oxide Structure for High-Performance Lithium-Ion Batteries. Advanced Functional Materials, 27 (22), 1700234-1-1700234-10.

Authors

Yunfeng Chao, Rouhollah Jalili, Yu Ge, Caiyun Wang, Tian Zheng, Kewei Shu, and Gordon G. Wallace

WILEY-VCH

DOI: 10.1002/ adfm.201700234
Article type: Full Paper

Self-assembly of Flexible Free-standing Three-Dimensional Porous MoS_2-Reduced Graphene Oxide Structure for High-performance Lithium-Ion Batteries

Yunfeng Chao, Rouhollah Jalili, Yu Ge, Caiyun Wang, Tian Zheng, Kewei Shu, Gordon G. Wallace**

Yunfeng Chao, Dr. Rouhollah Jalili, Yu Ge, Dr. Caiyun Wang, Tian Zheng, Kewei Shu, Prof. Gordon G. Wallace

ARC Centre of Excellence for Electromaterials Science, Intelligent Polymer Research Institute, AIIM Facility, Innovation Campus, University of Wollongong, NSW 2522, Australia.

E-mail: caiyun@uow.edu.au (C. W.), gwallace@uow.edu.au (G. G. W.)

Keywords: Lithium-ion batteries; MoS_2-graphene composites; Free-standing films; Three-dimensional porous structure; Self-assembly

Abstract: Flexible freestanding electrodes are highly desired if we are to realise wearable/flexible batteries as required for the design and production of flexible electronic devices. Here, the excellent electrochemical performance and inherent flexibility of atomically thin 2D MoS_2 along with the self-assembly properties of liquid crystalline graphene oxide (LCGO) dispersion are exploited to fabricate porous anode for high performance lithium ion batteries. Flexible free-standing MoS_2-reduced graphene oxide (MG)

film with a three dimensional (3D) porous structure was fabricated via a facile spontaneous self-assembly process and subsequent freeze-drying. This is the first report of a one pot self-assembly, gelation and subsequent reduction of MoS_2/LCGO composite to form a flexible, high performance electrodes for charge storage. The gelation process occurred directly in the mixed dispersion of MoS_2 and LCGO nanosheets at a low temperature (70 °C) and normal atmosphere (1 atm). The MG film with 75 wt% of MoS_2 exhibited a high reversible capacity of 800 mAh g^{-1} at a current density of 100 mA g^{-1}. It also demonstrated excellent rate capability, and excellent cycling stability with no capacity drop over 500 charge/discharge cycles at a current density of 400 mA g^{-1}.

1. Introduction

Transition metal dichalcogenide (TMD) materials are two-dimensional (2D) materials with a layered structure loosely held together by Van der Waals interactions. 2D MoS_2, a most studied member of this class of materials, demonstrates a variety of excellent properties such as flexibility, photoluminescence, direct bandgap and excellent electrochemical performance for applications in photo/electro-catalysts, transistors, energy storage & conversion devices.[1-3] There is a large interlayer distance of 0.65 nm between each S-Mo-S layer that allows insertion and intercalation of small atoms such as Li,[1, 4] which benefits the subsequent exfoliation of 2D MoS_2 and also the electrochemical intercalation/deintercalation of Li ion in lithium-ion batteries (LIBs). 2D MoS_2 possesses a high specific capacity of 670 mAh g^{-1},[3, 4] thus a promising anode material in LIBs.

Bulk MoS_2 crystal has a triangular prism structure (2H-MoS_2), which is a semi-conducting material[5] demonstrating poor rate capability. They are used as electrodes in combination with a conductive material, binder, and current collector. After exfoliation by organolithium, the crystalline structure is transformed to an octahedral structure (1T-MoS_2), exhibiting metallic properties with higher lithium storage capacity.[2, 5] However, the electrode based on

the exfoliated MoS_2 is not robust. The volume change encountered during cycling results in physical degradation of the MoS_2 sheets leading to capacity fading.[6] The aggregation of MoS_2 sheets and the side reaction between Li_2S and electrolyte during the charge-discharge process also leads to poor cycling stability.[6, 7]

The addition of carbon based materials forming composites with a 3D porous structure can effectively enhance the rate capability and cycling stability of MoS_2.[8] Among various carbon based materials, graphene or reduced graphene oxide has been the focus due to its large specific surface area, high conductivity, excellent processability and robustness of the final structure.[9-11] However, the realization of the ideal MoS_2/graphene structure in order to enhance electrochemical performance, mechanical robustness to ensure durability and stability remains elusive. The best structure should be a layered structure with MoS_2 sandwiched between graphene sheets, which could not only effectively enhance the electron transfer between MoS_2 sheets but also prevent aggregation of MoS_2 sheets during the discharge/charge processes. In addition, a 3D porous structure could be formed by the interconnected graphene sheets, which could tolerate the volume change of MoS_2 sheets and facilitate ion transport, giving rise to a greatly improved rate capability and cycling stability.[11, 12]

The large aspect ratio and excellent mechanical properties of graphene oxide sheets also allow for the formation of free-standing flexible MG films.[11] With no need for addition of binders or conductive additives dead weight and volume are eliminated.[13] Fabrication methods used to date include vacuum filtration,[14] templating method[4, 15] and self-assembly method[12, 16]. The filtration method usually produces compact MG films, in which MoS_2 sheets are prone to restack due to the non-intimate contact between graphene layers and MoS_2 layers.[12] The templating method usually involves a chemical vapor deposition (CVD) process producing 3D graphene foam template, which is at low efficiency and difficult for massive production. Self-assembly has been carried out via a hydrothermal process involving a high temperature

(180 °C for 24h) at the elevated pressure.[12] Very recently, a free-standing MG hydrogel has been obtained at a temperature of 80 °C,[16] yet a reducing agent thiourea was used in this process. In addition, a slicing and a subsequent compression process were required to form robust MG films for use.

In this regard, liquid crystalline dispersions of graphene oxide (LCGO), a processable form of graphene, holds great promise for self-assembly system due to the flexibility in processing, high unidirectional properties of the final architectures, and easy integration into complex layer-by-layer architectures.[10] Free-standing architectures from neat LCGO have been employed in high performance energy storage devices due to the large specific surface area, high conductivity, and excellent processability available and the robustness of the final structure.[17]

In the present work, we demonstrate that the key to producing such an ideal structure is the ability of ultra-large GO sheets to support formation of lyotropic LC phase in the presence of MoS_2 in order to create a dispersion suitable for subsequent composite formation. This approach enables the exploitation of the LC order of GO sheets to organize and align 2D MoS_2 in-between GO sheets. This work develops a simple, straightforward and cost-effective method to fabricate self-assembled, layer-by-layer, free-standing porous MG hydrogels from the mixed dispersion of MoS_2 and LCGO. Heating at 70 °C (overnight at 1 atm), followed by a freeze-drying process resulted in an electroactive, porous, flexible film that was used directly as an electrode. The structure displayed excellent electrochemical properties as a lithium-ion battery anode: a high discharge capacity of 800 mAh g^{-1} at a current density of 100 mA g^{-1}; and an excellent cycling stability with no capacity drop after 500 cycles at a current density of 400 mA g^{-1}.

2. Results and discussion

The aspect ratio (D/t) of LCGO sheets was estimated by dividing the average lateral size of the sheets (D) from SEM to the average sheet thickness (t) from AFM. Such exceptionally high aspect ratio (D/t in the range of 50,000) and flexibility of ultra-large sheets of LCGO provides a unique environment for matrix-guided molecular level self-assembly of nanomaterials.[18] Ultra-large Giant LCGO sheets were formed in the dispersion from exfoliated thermally expanded graphite (**Figure 1**a). The LCGO sheets with a large size of several micrometers are readily folded, as evidenced by the wrinkles observed, provided a large surface area and aspect ratio with excellent flexibility.[19] The thickness of a single-layer LCGO sheet is about 0.9 nm (Figure 1b), higher than the theoretical thickness of graphene (0.34 nm) due to the presence of oxygen-containing groups giving rise to this discrepancy.[11, 19] In contrast, MoS_2 sheets displayed a much smaller lateral size within tens of nanometers and lower aspect ratio (Figure 1c), which may be the reason for poor mechanical properties of the filtered MoS_2 film. The thickness of MoS_2 sheets is about 1 nm (Figure 1d), which is in accordance with the reported thickness for one single layer MoS_2 sheet, suggesting the successful exfoliation of MoS_2 powders in this work.[20] High resolution TEM images of LCGO and MoS_2 sheets (Figure 1e, f) were also collected, in which single-layer LCGO and MoS_2 sheets were revealed.

Figure 2 shows Cross-polarized optical microscope (POM) micrographs of different dispersions indicated that those containing MoS_2 alone were isotropic, however, the birefringence typical of a lyotropic nematic phase was observed with both LCGO alone as well as the LCGO dispersion containing MoS_2. Large areas of uniform orientation with random defects were observed, indicating full orientation of large LC domains. The high aspect ratio and the resultant large excluded volume of ultra-large GO sheets resulted in a very robust LC phase,[21, 22] which was found to accommodate significant amount of MoS_2 (75% by weight), while still maintaining LC order. This suggests that small size 2D MoS_2 nanosheets are sandwiched between large LCGO sheets forming an ordered layer-by-layer

structure as shown in the schematic of Figure 2d. This layer-by-layer structure was observed in transition electron detector images (Figure 2e and f). Comparing images of MoS_2/LCGO and LCGO it is evident that MoS_2 sheets were anchored on the surface of LCGO and embedded between large GO sheets forming an ordered layer-by-layer structure. By controlling the ratio and concentration of components in the dispersion, it was possible to control the self-assembly process to achieve a 2D MoS_2 distributed throughout and between LCGO sheets as a secondary material.

Formation of such self-assembled layer-by-layer structures in the liquid phase facilitates processing into practically useful structures. The superior aspect ratio of ultra-large LCGO sheets compared to 2D MoS_2 sheets not only facilitates the instantaneous surface assembly on the nanoscale level but also allows the entire architecture to remain stable in the liquid crystalline state for any subsequent process. Preserving this self-assembled structure was fundamental to formation of the MG hydrogel. A graphical representation of the gelation process and the free-standing electrodes fabricated are provided in Figure 2e. The gelation process occurred in the mixed MoS_2/LCGO dispersion at 70 ℃ and 1 atm overnight forming MG composites hydrogel. This type of hydrogel could also be formed at room temperature, but after at least 15 days. At the same conditions (70℃ and 1 atm overnight), no such gelation occurred in pure LCGO dispersion, while sedimentation was observed in pure MoS_2 dispersion as shown in Figure S1(see Supporting Information, SI). The understanding of self-assembly processes that occurr in formation of a layer-by-layer structure gives insights into the structure obtained. Repulsive interactions among charged GO sheets result in configurationally entropy driven excluded-volume effects. Above a critical concentration, the GO sheets orientate parallel to each other in order to minimize the volume excluded from the center-of-mass of the approaching sheet favoring LC phase.[19, 21] Equation S1 correlating formation of LC phase and the aspect ratio of the sheets was given in Supporting Information.

The high aspect ratio (in the range of 50,000) of LCGO sheets results in formation of LC at a very lower concentration (0.1 mg ml^{-1}).[19, 21]

The mixed MoS_2 and LCGO dispersion was transformed into a glass petri dish (mould), and a film-like MG hydrogel was formed. The size of the hydrogel was dictated by the ratio of the LCGO to MoS_2. Larger volume hydrogels can be obtained by using higher amounts of LCGO (Figure 2e), indicating the supporting role of LCGO. After a freeze-drying process, flexible MG films were obtained (Inset in Figure 2e). The dimensions of the formed hydrogel films is determined by the mould size and the dispersion precursor content.

As reported, MoS_2 sheets may anchor on the surface of LCGO sheets due to the electrostatic interactions between the functional oxygen-containing groups on LCGO and positively charged areas on the MoS_2 sheet.[23] This process would also reduce the repulsive force between large LCGO sheets, facilitating hydrogel formation. MoS_2 sheets tend to sediment in the acidic solution due to hydrogen ions disassociated from LCGO sheets.[24] Heating treatment (70 °C) enhances the interactions between LCGO and MoS_2 sheets as well as dehydration facilitating gel formation.

The XPS spectra of LCGO and MG75 films were de-convoluted to analyze the chemical structure changes (**Figure 3**).[25] In the C1s spectra of LCGO films, four peaks centered at 284.7, 285.6, 286.7 and 288.3 eV could be observed (Figure 3a), and are attributed to the sp^2 carbon (C-C), sp^3 carbon (C=C), and carbon in C-O bond and C=O bond, respectively.[26] These peaks were also observed for the LCGO film prepared by filtering LCGO dispersion (SI, Figure S2c). However, the intensity of C-O and C=O peaks for MG50 and MG75 films (Figure 3b-c) decreased dramatically, and MG75 with a higher MoS_2 content displayed the lowest intensity. The atomic ratio of carbon to oxygen (C/O) increased from 2.6 for the LCGO film to 3.43 for the MG50 film, and 5.22 for the MG75 film. These results clearly demonstrate that reduction of LCGO to form reduced graphene oxide (rGO) occurred, and that MoS_2 played an important role in this. In the Mo3d spectra of MG75 films (Figure 3d),

four peaks referring to Mo^{6+}, Mo $3d_{3/2}$, Mo $3d_{5/2}$ and S_{2s} peaks can be found.[27-29] The Mo^{6+} peak at 235.3eV corresponding to Mo-O can be ascribed to the oxidation of a small portion of Mo atoms.[28] The Mo $3d_{3/2}$ and Mo $3d_{5/2}$ peaks representing Mo^{4+} in MoS_2 could be further fitted into two peak doublets. The doublet at 232.8 and 229.4 eV is assigned to a 2H phase, while that at lower binding energy (231.8 and 228.6 eV) matches with 1T-MoS_2.[27-29] Clearly all the Mo3d XPS spectra (Figure 3d; SI, Figure S2a, b) demonstrate the domination of 1T-MoS_2 in both MoS_2 and MG films. Not surprisingly, the MG75 film prepared at room temperature after about 15 days displayed very similar XPS spectra (SI, Figure S2). LCGO showed a peak at 10.5° typical for graphene oxide materials in the XRD pattern (Figure S2f). MoS_2 displayed the peaks at 9.5° and 15.5° that can be indexed as expanded (002) and (004) planes of MoS_2 as previously reported.[27] A new broad peak at 23° appeared for the MG75 film, and this can be attributed to the (002) plane of rGO.

MG and MoS_2 films all displayed two characteristic peaks in the Raman spectra (Figure 3e): E^1_{2g} (380 cm^{-1}) and A_{1g} (405 cm^{-1}). The E^1_{2g} derives from the symmetric vibration of S atoms opposite to Mo atom within the S-Mo-S layer, while A_{1g} peak is related to the out-of-plane vibration of two S atoms in the opposite directions.[28] The appearance of D band at 1342.2 cm^{-1} and G band at 1593.1 cm^{-1} indicates the co-existence of sp^3 defective and disordered carbon, and sp^2 2D graphite carbon in the contained rGO. They are attributed to the breathing mode of A_{1g} symmetry (D band) and first-order scattering of E_{2g} phonons (G band), respectively.[11, 30] The intensity ratio of D band to G band (I_d/I_g) was slightly increased from 1.18 for LCGO film to 1.27 for MG50 film, which could be explained by the formation of a 3D structure with more defects from the edges,[11, 28] while a drop of I_d/I_g to 1.024 for MG75 film is attributed to a further reduction of sp^3 to sp^2.[31]

The thermal degradation of MoS_2, LCGO and composite films was compared using TGA (Figure 3f). For LCGO, two typical weight loss stages were observed: removal of functional oxygen-containing groups on LCGO nanosheets over the range of 180-210 ℃, LCGO

decomposition forming carbon dioxide after 530 °C.[32] For pure MoS_2 film, the major decomposition started from 450 °C that was caused by the oxidation of MoS_2 to MoO_3.[29, 33] After heating to 600 °C, the weight losses were 100%, 29%, 67% and 50% for LCGO, MoS_2, MG50 and MG75 films, respectively. The loading amounts of MoS_2 were estimated to be 70.4% and 46.5% for MG75 film and MG50 film, which was in good agreement with the initial ratios.

To observe the geometrical effects of the self-assembly, gelation, low temperature reduction and subsequent freeze-drying on the final 3D architectures, FESEM microscopy was performed (**Figure 4**a-c). Both MG50 and MG75 films displayed a uniformly interconnected 3D porous structure with the pore size of several micrometers, as revealed by their cross-sectional view and surface morphology. The elements distribution in the representative MG75 film was investigated. The uniform distribution of C, O, Mo and S elements (Figure 4e-h) verifies the formation of a hybrid structure.[23] They also indicate that 2D MoS_2 sheets are homogeneously distributed both on the surface and in-between the LCGO sheets, bridging them together and thus creating a highly conductive 3D network architecture. Such an ordered porous structure was formed associated with the nematic liquid crystalline phase formed in the mixed MoS_2/LCGO dispersion induced by large-size LCGO nanosheets.[10, 21] The formed ordered structure was retained during the freeze-drying process. Moreover, the introduction of 2D MoS_2 between graphene sheets prevents agglomeration, leaving sufficient space for electrolyte penetration and potentially resulting in high performance. The cross-sectional SEM images of LCGO and MoS_2 films and their elements mapping images are shown in Figure S4 (SI). The freeze-dried pure LCGO film presented a porous structure, while the pure MoS_2 film showed a compact layered structure due to the re-stack and arrangement of 2D nanosheets during the filtration process. It was brittle and hard to handle, which can be ascribed to the small size of MoS_2 sheets and weak Van der Waals force in-between these sheets.

The first cathodic CV scan of a MG75 film (**Figure 5**a) displayed four peaks. The broad peak around 1.75 V can be attributed to the reduction of oxygen-containing functional groups remaining on the reduced graphene oxide sheets, in accordance with the large peak at 1.55 V observed in the first discharge curve of LCGO film (SI, Figure S5c).[34] The small cathodic peak at about 0.95 V can be attributed to the intercalation of lithium ions into the triangular prism structure of MoS_2, forming Li_xMoS_2 with an octahedral structure.[26, 35] The smaller peak at 0.65 V corresponds to the formation of a solid electrolyte interface (SEI),[36] while the peak at 0.40 V represents the reduction of Li_xMoS_2 that based on the conversion reaction

$Li_xMoS_2 + (4\text{-}x)\ Li^+ + (4\text{-}x)\ e^- \rightarrow Mo + 2Li_2S$.[26, 37]

All four peaks disappered in the following cycles, and two new reduction peaks at 1.80 V and 1.0 V appeared, and they can be attributed to formation of Li_2S and Li_xMoS_2 according to:

$2Li^+ + S + 2e^- \rightarrow Li_2S$;

$MoS_2 + x\ Li^+ + x\ e^- \rightarrow Li_xMoS_2$.[35, 37]

During the charging process, there are a broad anodic peak centered at about 1.55 V and a peak at 2.40 V, which could be assigned to the partial oxidation of Mo atoms and the delithiation process

Li_2S: $Li_2S \rightarrow 2Li^+ + S + 2e^-$.[26]

These two peaks were in accordance with the peaks for MoS_2 film (SI, Figure S5a), providing further evidence of their origin. The almost over-lapped CV curves at the second and third scans indicates good reversibility.[4]

The first three discharge-charge curves of MG75, MoS_2 and LCGO films at a current density of 100 mA g^{-1} were recordeed (SI, Figure S5d). The plateaus are inconspicuous for MG75 film in the first discharge process, which is in accordance with those four weak peaks in the first CV scan. Both MG75 and MoS_2 films displayed two obvious plateaus in the following cycles, which matched well with those two strong peaks in the CV curves. The plateau at ~2.40 V during charging and that at 1.80 V during discharging represent the formation and

delithiation process of Li_2S, respectively. MG75 film delivered an initial capacity of 984 mAh g^{-1} and a high reversible capacity of 786 mAh g^{-1}. The irreversible capacity in the first cycle may be attributed to the formation of SEI, reduction of the remained oxygen-containing functional groups on graphene sheets, and some lithium trapped in defect sites.[15, 37] In contrast, pure MoS_2 film had a slightly lower initial discharge capacity of 875 mAh g^{-1} but a much lower reversible capacity of 631.5 mAh g^{-1}. The initial coulombic efficiency of MG75 film is 80%, much higher than that for MG50 (72%), GO (49%) and MoS_2 film (72%). The high efficiency from MG75 can be attributed to lithium ions trapped in the porous structure.[38]

The MG75 film delivered a much higher capacity at all the applied current densities investigated (from 100 mA g^{-1} to 1 A g^{-1}), compared to MG50, MoS_2 and LCGO films (Figure 5d). It was 799, 658, 526, 401 and 350 mAh g^{-1} at a current density of 100, 200, 400, 800 and 1000 mA g^{-1}, respectively. In contrast, MoS_2 film delivered a much lower capacity of 508, 356, 189, 95 and 75.4 mAh g^{-1}; an even lower capacity of 160,127, 95, 67 and 59 mAh g^{-1} was delivered from LCGO film. This MG75 film displayed a slightly higher capacity at 100 mA g^{-1} than the reported for rGO@MoS_2 nanocomposites[28]: 786 mAh g^{-1}, and 650 mAh g^{-1} for MoS_2/C composites[39]. Using a higher current density (1 A g^{-1}), the difference in perfromance over previous work was accelerated, it delivered a much higher capacity of 350 mAh g^{-1} in sharp contrast to 158 mAh g^{-1} [28], and 260 mAh g^{-1} [39] previously reported. The MG75 electrode delivered a capacity of 745 mAh g^{-1} when the current was reverted to 100 mA g^{-1}, very close to its initial capacity of 799 mAh g^{-1}, confirming good reversibility.[2] In contrast, MoS2 electrode delivered a capacity of 400 mAh g^{-1}, only 79% of the initial capacity. All these results clearly demonstrate the excellent rate capability of the MG75 electrode. Graphene sheets act as highly conducting pathway for electron movement, but more importantly, MoS_2 inhibit the restacking of the graphene sheets, thus increasing the effective surface area and number of ion exchange channels for the electrochemical reactions.

The cycling stability of these electrodes (Figure 5e) was evaluated at a current density of 400 mA g^{-1}. MG75 film only showed a slight discharge capacity drop from 400 mAh g^{-1} to 357.4 mAh g^{-1} after the first 35 cycles, yet increased gradually to 450 mAh g^{-1} over 500 cycles. A similar trend was also found for LCGO film, the capacity increased from 90 to 125 mAh g^{-1} over 500 cycles. This may be attributed to the reduction of GO during the cycling test. In contrast, the MoS_2 electrode has an obvious capacity decrease from 250 mAh g^{-1} to only 150 mAh g^{-1} over 500 cycles, probably due to the deconstruction of MoS_2 nanosheets and the shuttle effect of polysulfides.[3, 40] The coulombic efficiency of MG75 reached 98% in the third cycle and stabilized between 98-100% till the 500th cycle, illustrating its high coulombic efficiency and cycling stability. These excellent electrochemical properties may be derived from the synergistic effects between MoS_2 and rGO nanosheets. Firstly, the introduction of conductive rGO increased the conductivity of MG75 film enhancing the rate capability. The robust rGO nanosheets could effectively tolerate the volume change and prevent the restacking of MoS_2 nanosheets during cycling, improving the cycling performance same as reported for $MoSe_2$/graphene foam composites[41]. The 3D porous structure also increased the interface between electrolyte and electrode materials facilitating ion diffusion for high capacity and good rate capability.

On top of that, over prolonged cycling, the ordered stack of ultra-large graphene sheets pushes small 2D MoS_2 sheets to rearrange themselves to achieve higher level of orders.[21] In other word, in the ordered composite containing ultra-large GO sheets and much smaller 2D MoS_2 sheets, the bigger sheets generate driving force for smaller sheets for entropic rearrangement to form long range ordering. The presence of ultra-large sheets in our system, therefore, limits the movement of small 2D MoS_2 sheets and pushes them toward higher level of ordering over the contraction and expansion (cycling). This resulted in gradual introduction of new micro channels for electrolyte ions and contributed to a higher intercalation of lithium ions. This phenomenon is unique in our system and resulted in an increased capacity over prolonged

cycling rather than a decrease. Table S1 compared the cycling stability of MG75 film prepared from LC rout in this study against previous reports on the state-of-art MG composites. A capacity fade could be observed in almost all the reports even for those subjected to a low number of 80 cycles. The close to perfect layer-by-layer structure presented here overcomes this challenge by utilizing soft self-assembly fabrication route along with high mechanical stability of ultra-large graphene sheets. Such high performances, excellent cycle stability in conjunction with ease of preparation make these architectures an ideal candidate for applications in flexible anode material in LIBs.

The Nyquist plots of MG75, MoS_2 and LCGO films were collected (**Figure 6**) after the rate capability and cycling stability test, and fitted using an equivalent circuit model (Figure 6d). The slope of the line at low frequency is related to Li^+ diffusion into electrode materials, while the semicircle at high frequency region indicates the contact resistance and charge transfer resistance at the interface between electrode and electrolyte. In the equivalent circuit, R_s, R_{ct}, CPE and Z_w represents contact resistance, charge transfer resistance, double layer capacitance and Warburg impedance, respectively.[42] The R_{ct} of LCGO film decreased from 255 Ω to 142 Ω after the cycling test, which can be ascribed to the deep reduction of LCGO during cycling. These results provide the evidence for the increased capacity demonstrated in the cycling stability test. The R_{ct} of MoS_2 film increased from 212 Ω to 241 Ω, which may be attributed to the restacking of MoS_2 nanosheets. This also explained its poor rate capability and cycling performance.[40] Not surprisingly, the MG75 film possesses the lowest charge transfer resistance (148 Ω), which can be attributed to the doping of conductive rGO. After the cycling test, R_{ct} of MG75 film was further dropped to 135 Ω, illustrating the deep reduction of rGO and introduction of new micro channels. It also indicates that no restacking problems occurred in MG75 film due to the introduction of rGO nanosheets and the stable 3D porous structure constructed.

3. Conclusion

A self-assembled, flexible free-standing MoS_2-reduced graphene oxide composite films with a 3D porous structure was fabricated, employing a novel yet facile soft self-assembly fabrication route. The MG hydrogel can be formed from a mixed dispersion of MoS_2 and graphene oxide nanosheets. A birefringent lyotropic LC behavior is observed in this mixed dispersion, evidence of an ordered self-assembly structure which is the fundamental to the MG hydrogel formation. The approach is readily scalable and cost effective and can be used to produce multifunctional flexible 3D electrodes. This MG electrode demonstrated a greatly enhanced performance, including high capacity, good rate capability and cycling stability, compared to LCGO and MoS_2 films. Such enhancement can be ascribed to the synergistic effect between these two components and gradual perfection of the ordered structure. It is also clear that our method can be easily expanded for massive production. This work may provide a new avenue for the development of 3D porous flexible composite electrode materials with high performance using the unique LCGO.

4. Experimental Section

Preparation of liquid crystalline graphene oxide (LCGO) dispersion: LCGO was prepared by a modified Hummer's method using thermal expanded graphite (EG).[19] Briefly, EG was synthesized by heating expandable graphite flakes (3772, Asbury Graphite Mills) at 1050 ℃ for 15 s. The formed EG (2 g) was added into concentrated sulfuric acid (400 ml) in a three-neck flask and being stirred for 24 hours, followed by addition of $KMnO_4$ (15 g) and kept stirring for another 24 hours. Milli-Q water (400 ml) was added slowly into this reaction mixture in an ice bath and kept it stirred for 1 hour. A color change from black to light brown could be observed along with the introduction of H_2O_2 (30%, 100 ml). This dispersion was subjected to repeatedly rinsing with 10 fold diluted HCl solution (4.2 wt%) and Milli-Q water until its PH was ~5. Then a LCGO dispersion with large graphene oxide sheets was obtained, and it was diluted to 2 mg/ml for future use.

Preparation of MoS_2 dispersion: Exfoliated MoS_2 dispersion was synthesized by a lithium-intercalated process.[43] Briefly, 1 g of molybdenum disulfide (99%, Alfa Aesar) in a round-bottom flask was dried in an oven at 120 ℃ for 2 hours. Under the protection of argon, 10 ml of n-butylithium (n-Bu-Li, 2.5 M in hexanes, Sigma-Aldrich) was injected into the flask and kept it stirred for 48 h forming Li_xMoS_2.[50] The resultant dispersion was being sonicated for 1 hour, followed by a slow addition of Milli-Q water (100 ml) producing exfoliated MoS_2 sheets. The chemical reactions involved are:

$$MoS_2 \xrightarrow{n-BuLi} Li_xMoS_2 \xrightarrow{H_2O} MoS_2 \text{ (monolayer sheets)} + LiOH + H_2.$$[23, 44]

This dispersion was dialyzed in water for more than 1 week to remove the residual chemicals. The MoS_2 dispersion needs to be sonicated for 1 hour prior to the use.

Synthesis of MG aerogel/film: The MoS_2 and LCGO dispersion with the same concentration (2 mg/ml) was mixed by a vortex mixer for 10 minutes in a vial. A MG hydrogel was formed after heating at 70 ℃ in an oven overnight. When the mixed dispersion was transferred into a glass petri dish with an acrylic plate cover, a film-like MoS_2/LCGO hydrogel was formed at the same conditions. This film was rinsed with distilled water for 3 times, followed by a freezing dry process forming porous MoS_2/LCGO film.

The total weight of MoS_2 and LCGO in the dispersion was kept constant. The film formed was named according to the percentage of MoS_2. The film produced with equal amount of MoS_2 dispersion and LCGO dispersion (8 ml each) was labelled as MG50 film, while the one from 12 ml of MoS_2 and 4 ml of LCGO was designated as MG75 film. No free-standing MG films could be formed if the amount of LCGO was further reduced. As control samples, pure LCGO and MoS_2 films were prepared by filtering their dispersions processing under same conditions as that for MG film. The LCGO film was freeze-dried, while MoS_2 film was dried in an oven at 60 ℃ due to its poor mechanical properties.

Material characterizations: The exfoliated LCGO and MoS_2 nanosheets were deposited on the pre-cleaned mica plate to collect their topographic data by atomic force microscope (AFM, Asylum Research, MFP-3D). Transmission electron microscopy (TEM) images of these nanosheets were collected using JEOL JEM-2200FS. The birefringence of dispersions was examined by polarized optical microscopy (POM, Leica CTR 6000) operated in transmission mode by observing a drop of dispersion on a glass slide. X-ray photoelectron spectroscopy (XPS) data was recorded using a hemispherical energy PHOIBOS 100/150 analyzer. Raman spectra were performed with a confocal Raman spectrometer (Jobin Yvon HR800, Horiba) using 632.8 nm diode laser. Thermogravimetric analysis (TGA) was conducted on a Pyris Diamond thermogravimetric/differential thermal analyzer at a heating rate of 5 °C min^{-1} in air flow. Field emission scanning electron microscopy (FE-SEM, JEOL JSM-7500FA) was used to characterize the morphology, while the energy dispersive spectroscopy (EDS) was applied to analyze the element distribution.

Electrochemical measurement: After drying in a vacuum oven at 60 °C overnight, a MG film was assembled into a LR 2032 coin cell with a lithium foil as counter and reference electrode in an argon-filled glovebox (MBrau, UNIlab Plus). The electrolyte used was 1 M $LiPF_6$ in a mixture of ethylene carbonate (EC) and dimethyl carbonate (DMC) (1:1, v/v) (Aldrich). Cyclic voltammetry (CV) was conducted from 0.01 to 3 V (vs. Li/Li^+) using a Solartron SI 1287 electrochemical system at a scan rate of 0.2 mV s^{-1}. Galvanostatic charge/discharge tests were carried out between 0.005 and 3 V (vs. Li/Li^+) using a LAND CT2001A battery test system (Wuhan Jinnuo Electronics Co. Ltd.). Electrochemical impedance spectra (EIS) was measured using a Gamry EIS 3000 system over the frequency range of 100 kHz to 0.01 Hz with an AC perturbation of 10 mV.

Supporting Information

Supporting Information is available from the Wiley Online Library or from the author.

Acknowledgements
Funding from the Australian Research Council Centre of Excellence Scheme (Project Number CE 140100012) is gratefully acknowledged. G.G.W. is grateful to the ARC for support under the Australian Laureate Fellowship scheme (FL110100196). The authors would like to thank the Australian National Nanofabrication Facility-Materials node (ANFF) and the UOW Electron Microscopy Centre for equipment use. Y. C. acknowledges the support of the CSC scholarship from the Ministry of Education of P. R. China.

Received: ( )
Revised: ( )
Published online: ( )

References

[1] N. A. Kumar, M. A. Dar, R. Gul, J. B. Baek, *Mater. Today* **2015**, *18*, 286.

[2] M. Yang, S. Ko, J. S. Im, B. G. Choi, *J. Power Sources* **2015**, *288*, 76.

[3] S. K. Das, R. Mallavajula, N. Jayaprakash, L. A. Archer, *J. Mater. Chem.* **2012**, *22*, 12988.

[4] J. Wang, J. Liu, D. Chao, J. Yan, J. Lin, Z. X. Shen, *Adv. Mater.* **2014**, *26*, 7162.

[5] M. Acerce, D. Voiry, M. Chhowalla, *Nat. Nanotechnol.* **2015**, *10*, 313.

[6] Z. Hu, Q. Liu, W. Sun, W. Li, Z. Tao, S. Chou, J. Chen, S. Dou, *Inorg. Chem. Front.* **2016**, *3*, 532.

[7] X. Li, J. Zai, S. Xiang, Y. Liu, X. He, Z. Xu, K. Wang, Z. Ma, X. Qian, *Adv. Energy Mater.* **2016**, 1601056.

[8] a) S. H. Choi, Y. N. Ko, J. K. Lee, Y. C. Kang, *Adv. Funct. Mater.* **2015**, *25*, 1780; b) J. Xiang, D. Dong, F. Wen, J. Zhao, X. Zhang, L. Wang, Z. Liu, *J. Alloys Compd.* **2016**, *660*, 11.

[9] a) S. Gambhir, R. Jalili, D. L. Officer, G. G. Wallace, *NPG Asia Mater.* **2015**, *7*, e186; b) D. Esrafilzadeh, R. Jalili, E. M. Stewart, S. H. Aboutalebi, J. M. Razal, S. E. Moulton, G. G. Wallace, *Adv. Funct. Mater.* **2016**, *26*, 3105.

[10] R. Jalili, S. H. Aboutalebi, D. Esrafilzadeh, K. Konstantinov, S. E. Moulton, J. M. Razal, G. G. Wallace, *ACS Nano* **2013**, *7*, 3981.

[11] K. Shu, C. Wang, S. Li, C. Zhao, Y. Yang, H. Liu, G. Wallace, *J. Mater. Chem. A* **2015**, *3*, 4428.

[12] D. Xie, W. Tang, X. Xia, D. Wang, D. Zhou, F. Shi, X. Wang, C. Gu, J. Tu, *J. Power Sources* **2015**, *296*, 392.

[13] a) C. Wang, G. G. Wallace, *Electrochim. Acta* **2015**, *175*, 87; b) I. Sultana, M. M. Rahman, J. Wang, C. Wang, G. G. Wallace, H. Liu, *Electrochim. Acta* **2012**, *83*, 209.

[14] a) L. David, R. Bhandavat, G. Singh, *ACS nano* **2014**, *8*, 1759; b) R. Wang, C. Xu, J. Sun, Y. Liu, L. Gao, H. Yao, C. Lin, *Nano Energy* **2014**, *8*, 183.

[15] J. Wang, J. Liu, J. Luo, P. Liang, D. Chao, L. Lai, J. Lin, Z. Shen, *J. Mater. Chem. A* **2015**, *3*, 17534.

[16] W. S. Lee, E. Peng, T. A. Loh, X. Huang, J. M. Xue, *Nanoscale* **2016**, *8*, 8042.

[17] a) S. H. Aboutalebi, R. Jalili, D. Esrafilzadeh, M. Salari, Z. Gholamvand, S. Aminorroaya Yamini, K. Konstantinov, R. L. Shepherd, J. Chen, S. E. Moulton, P. C. Innis, A. I. Minett, J. M. Razal, G. G. Wallace, *ACS Nano* **2014**, *8*, 2456; b) K. M. Kim, J. A. Lee, H. J. Sim, K. A. Kim, R. Jalili, G. M. Spinks, S. J. Kim, *Nanoscale* **2016**, *8*, 1910.

[18] a) K. S. U. Schirmer, D. Esrafilzadeh, B. C. Thompson, A. F. Quigley, R. M. I. Kapsa, G. G. Wallace, *J. Mater. Chem. B* **2016**, *4*, 1142; b) P. Poulin, R. Jalili, W. Neri, F. Nallet, T. Divoux, A. Colin, S. H. Aboutalebi, G. Wallace, C. Zakri, *Proc. Nati. Acad. Sci.* **2016**, *113*, 11088.

[19] R. Jalili, S. H. Aboutalebi, D. Esrafilzadeh, R. L. Shepherd, J. Chen, S. Aminorroaya Yamini, K. Konstantinov, A. I. Minett, J. M. Razal, G. G. Wallace, *Adv. Funct. Mater.* **2013**, *23*, 5345.

[20] a) J. Zheng, H. Zhang, S. Dong, Y. Liu, C. T. Nai, H. S. Shin, H. Y. Jeong, B. Liu, K. P. Loh, *Nat. commun.* **2014**, *5*; b) Z. Zeng, Z. Yin, X. Huang, H. Li, Q. He, G. Lu, F. Boey, H. Zhang, *Angew. Chem. Int. Ed.* **2011**, *50*, 11093.

[21] R. Jalili, S. H. Aboutalebi, D. Esrafilzadeh, K. Konstantinov, J. M. Razal, S. E. Moulton, G. G. Wallace, *Mater. Horizons* **2014**, *1*, 87.

[22] M. M. Islam, S. H. Aboutalebi, D. Cardillo, H. Liu, K. Konstantinov, S. Dou, *ACS Cent Sci.* **2015**, *1*, 206.

[23] Y. Liu, Y. Zhao, L. Jiao, J. Chen, *J. Mater. Chem. A* **2014**, *2*, 13109.

[24] A. S. Goloveshkin, I. S. Bushmarinov, N. D. Lenenko, M. I. Buzin, A. S. Golub, M. Y. Antipin, *J. Phys. Chem. C* **2013**, *117*, 8509.

[25] Y. Ge, C. Wang, K. Shu, C. Zhao, X. Jia, S. Gambhir, G. G. Wallace, *RSC Adv.* **2015**, *5*, 102643.

[26] Y. Jing, E. O. Ortiz-Quiles, C. R. Cabrera, Z. Chen, Z. Zhou, *Electrochim. Acta* **2014**, *147*, 392.

[27] Z. Shi, W. Kang, J. Xu, Y. Sun, M. Jiang, T. W. Ng, H. Xue, D. Y. W. Yu, W. Zhang, C. S. Lee, *Nano Energy* **2016**, *22*, 27.

[28] H. Liu, X. Chen, L. Deng, X. Su, K. Guo, Z. Zhu, *Electrochim. Acta* **2016**, *206*, 184.

[29] Y. Xia, B. Wang, X. Zhao, G. Wang, H. Wang, *Electrochim. Acta* **2016**, *187*, 55.

[30] A. K. Das, M. Srivastav, R. K. Layek, M. E. Uddin, D. Jung, N. H. Kim, J. H. Lee, *J. Mater. Chem. A* **2014**, *2*, 1332.

[31] G. T. S. How, A. Pandikumar, H. N. Ming, L. H. Ngee, *Sci. Rep.* **2014**, *4*, 5044.

[32] Y. Wang, J. Liu, L. Liu, D. D. Sun, *Nanoscale Res. Lett.* **2011**, *6*, 1.

[33] N. Kapil, A. Singh, M. Singh, D. Das, *Angew. Chem. Int. Ed.* **2016**, *55*, 7772.

[34] a) K. Shu, C. Wang, M. Wang, C. Zhao, G. G. Wallace, *J. Mater. Chem. A* **2014**, *2*, 1325.

[35] H. Wang, D. Ren, Z. Zhu, P. Saha, H. Jiang, C. Li, *Chem. Eng. J.* **2016**, *288*, 179.

[36] J. He, C. Zhang, H. Du, S. Zhang, P. Hu, Z. Zhang, Y. Ma, C. Huang, G. Cui, *Electrochim. Acta* **2015**, *178*, 476.

[37] G. Huang, T. Chen, W. Chen, Z. Wang, K. Chang, L. Ma, F. Huang, D. Chen, J. Y. Lee, *Small* **2013**, *9*, 3693.

[38] Z. Li, Q. He, L. He, P. Hu, W. Li, H. Yan, X. Peng, C. Huang, L. Mai, *J. Mater. Chem. A* **2017**, DOI: 10.1039/C6TA10583A.

[39] X. Chen, L. Li, S. Wang, C. Feng, Z. Guo, *Mater. Lett.* **2016**, *164*, 595.

[40] H. Shu, F. Li, C. Hu, P. Liang, D. Cao, X. Chen, *Nanoscale* **2016**, *8*, 2918.

[41] J. Yao, B. Liu, S. Ozden, J. Wu, S. Yang, M. T. F. Rodrigues, K. Kalaga, P. Dong, P. Xiao, Y. Zhang, R. Vajtai, P. M. Ajayan, *Electrochim. Acta* **2015**, *176*, 103.

[42] Y. Li, L. Kong, M. Liu, W. Zhang, L. Kang, *Mater. Lett.* **2017**, *186*, 289.

[43] R. Jalili, S. Aminorroaya-Yamini, T. M. Benedetti, S. H. Aboutalebi, Y. Chao, G. G. Wallace, D. L. Officer, *Nanoscale* **2016**, *8*, 16862.

[44] A. Ambrosi, Z. Sofer, M. Pumera, *Small* **2015**, *11*, 605.

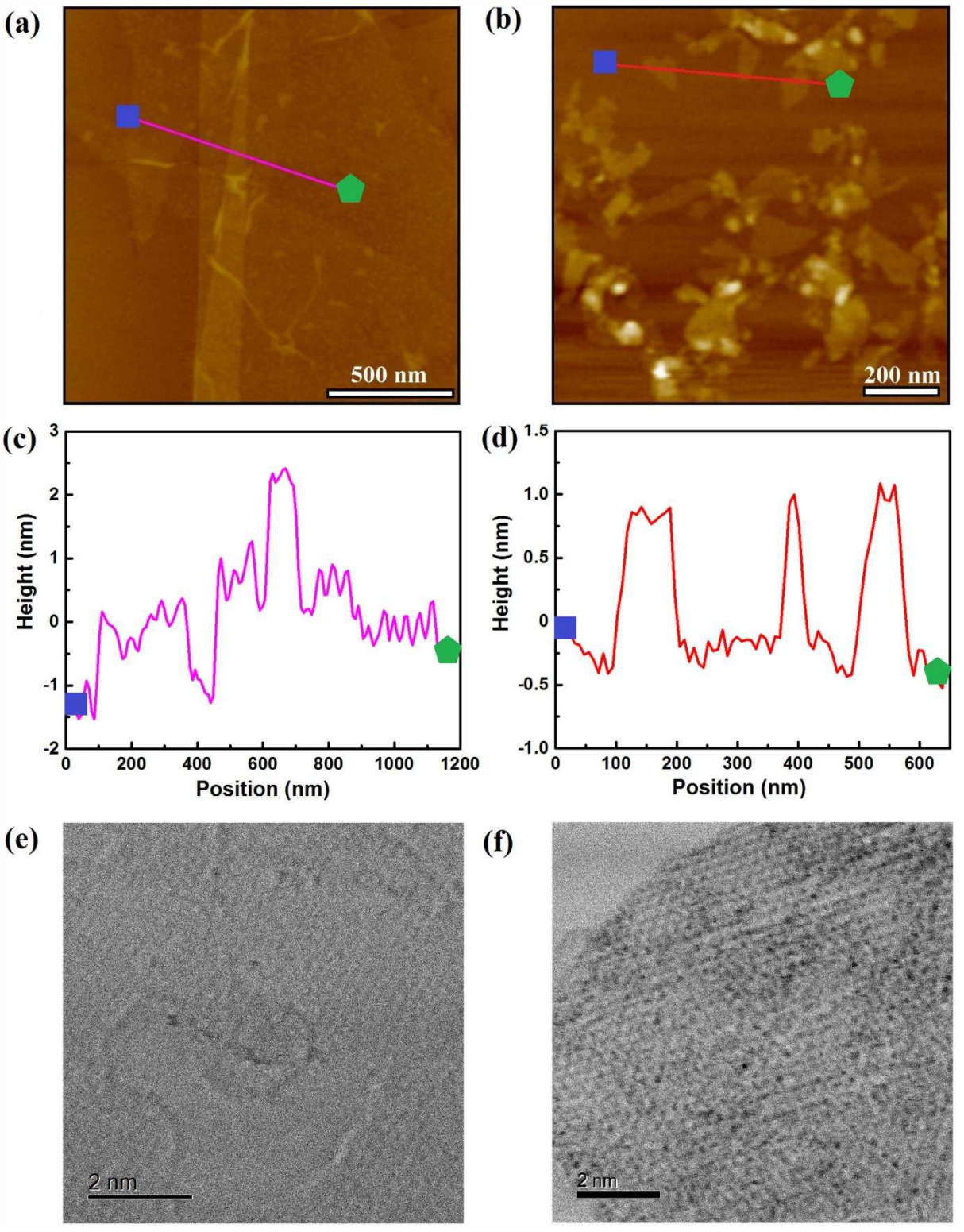

Figure 1. AFM images and height profiles of exfoliated LCGO (a, c) and MoS_2 sheets (b, d); High resolution TEM images of exfoliated LCGO (e) and MoS_2 sheets (f).

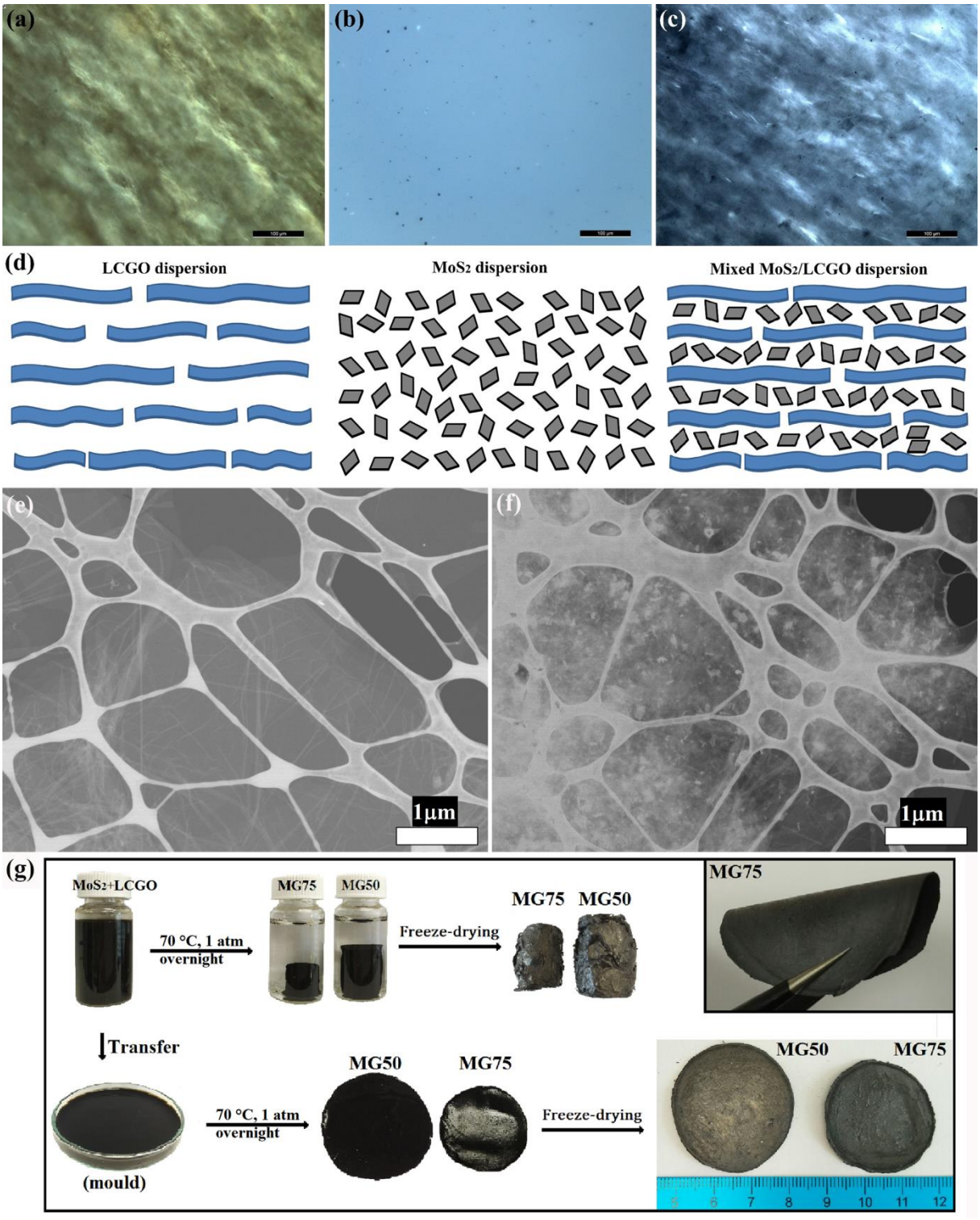

Figure 2. POM images of LCGO dispersion (a), MoS_2 dispersion (b) and mixed MoS_2/LCGO dispersion (c); (d) Schematic structure of those three dispersions; Transition electron detector (TED) images of LCGO (e) and MoS_2/LCGO (f); (g) Schematic procedure to fabricate MG composites hydrogels including photos of the formed MG foams and films, flexibility demonstration of MG75 film.

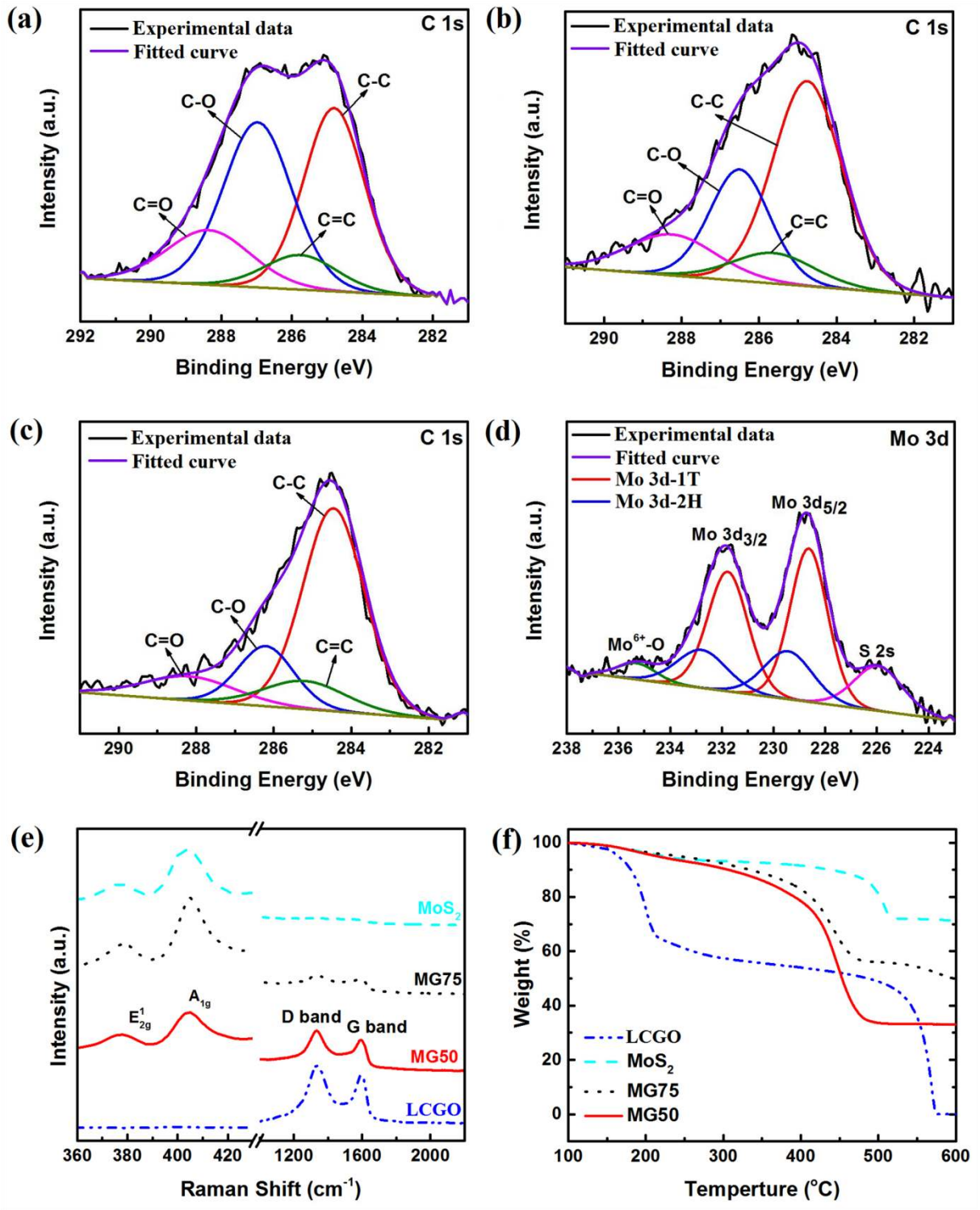

Figure 3. XPS spectra of the LCGO film (a), MG50 film (b) and MG75 film (c-d); Raman spectra (e) and TGA curves (f) of MG, LCGO and MoS_2 films.

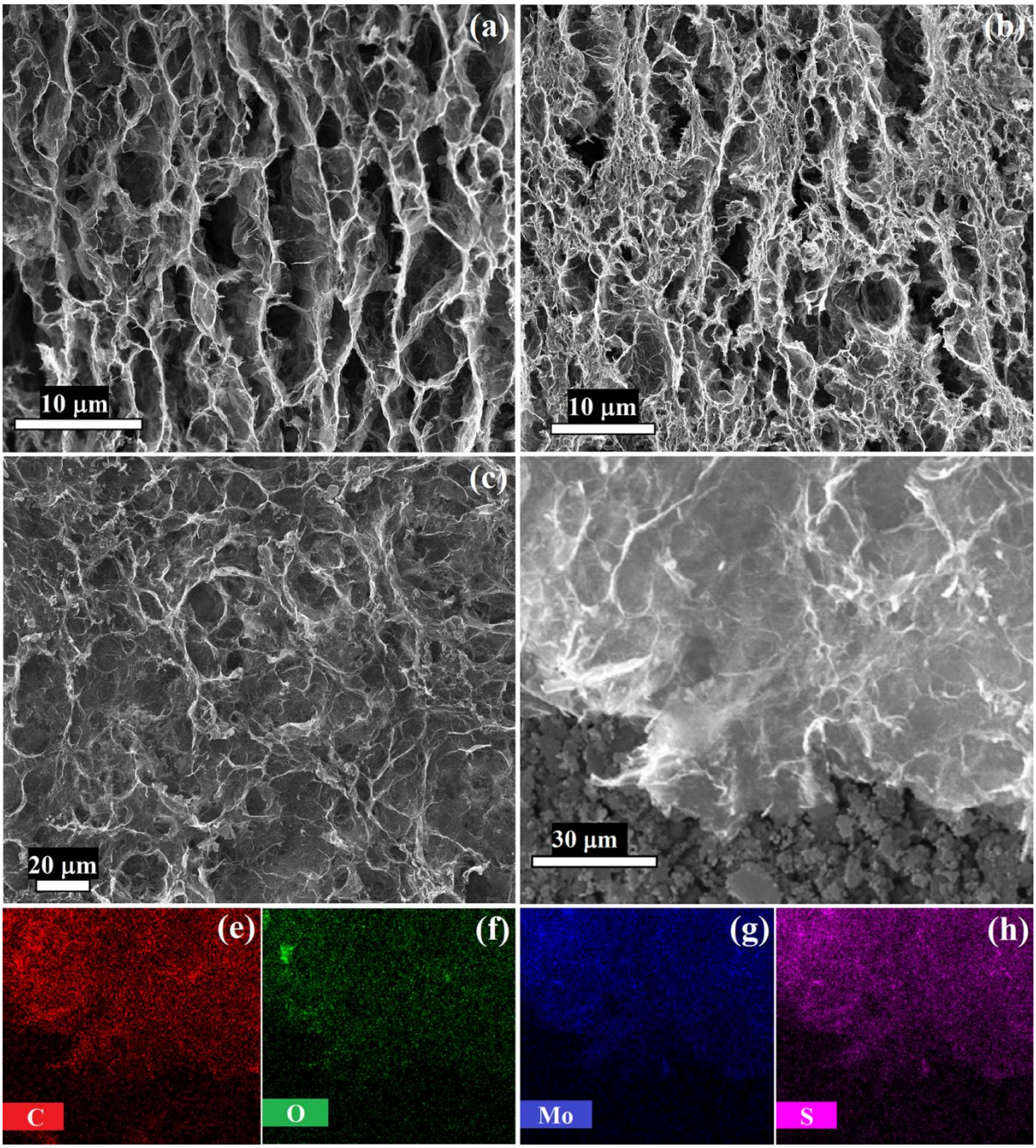

Figure 4. Cross-sectional SEM images of MG50 film (a) and MG75 film (b); Surface morphology of MG75 film (c); Area used for the element mapping (d) and the EDS mapping of elements C (e), O (f), Mo (g) and S (h).

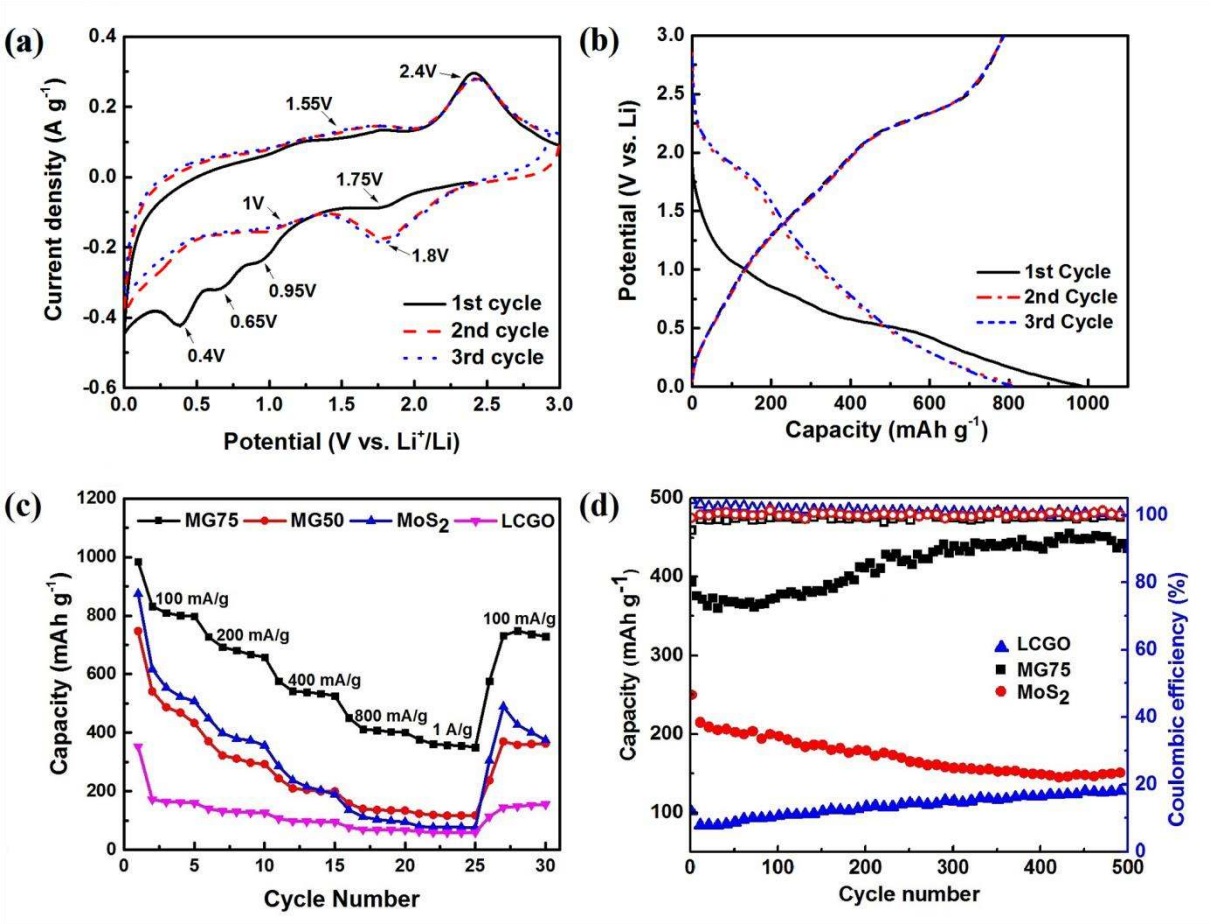

Figure 5. (a) The first three cyclic voltammograms of MG75 film at a scan rate of 0.2 mV s^{-1}; (b) The first three discharge/charge curves of MG75 film at a current density of 100 mA g^{-1} over a potential range of 0.005 to 3V; (c) Rate capability of MG, LCGO and MoS_2 films; (d) Cycling stability of LCGO, MG75 and MoS_2 films at a current density of 400 mA g^{-1} (Labels: solid for capacity; hollow for coulombic efficiency).

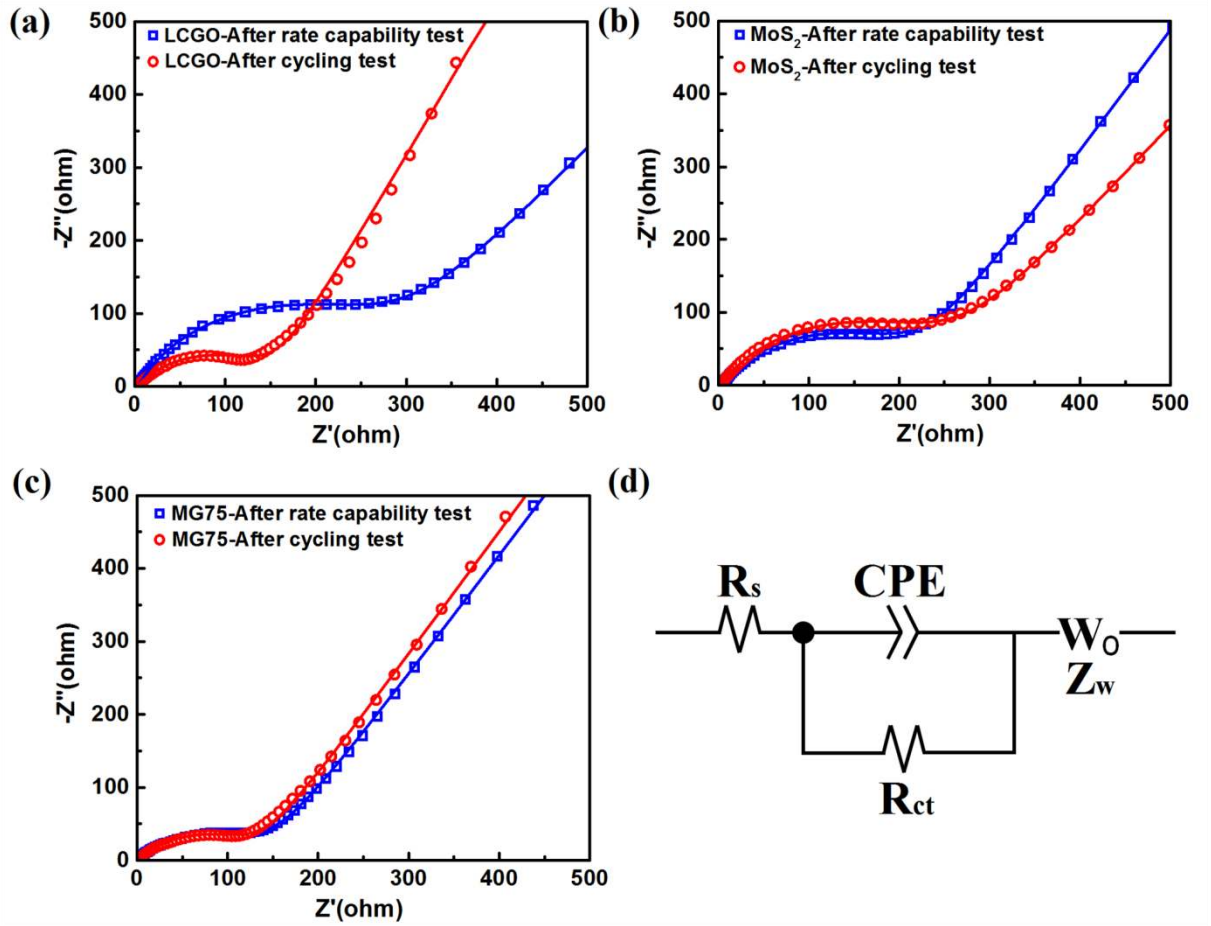

Figure 6. Nyquist plots (symbols) and simulation curves (lines) of LCGO (a), MoS_2 (b), and MG75 (c) films at the open circuit potential over the frequency range of 100 kHz to 10 mHz; (d); An equivalent circuit used to fit the Nyquist plots.

A flexible free-standing porous MoS_2-graphene film is fabricated via a facile spontaneous self-assembly process and subsequent freeze-drying. The birefringent lyotropic liquid crystalline behavior in the precursor faciliates the hydrogel formation. The film produced exhibited greatly improved electrochemical properties in lithium-ion batteries. This work may provide a new avenue for the development of flexible composite electrodes.

Keyword: Lithium-ion batteries; MoS_2-graphene composites; Free-standing films; Three-dimensional porous structure; Self-assembly

Yunfeng Chao, Rouhollah Jalili, Yu Ge, Caiyun Wang*, Tian Zheng, Kewei Shu, Gordon G. Wallace*

Self-assembly of Flexible Free-standing Three-Dimensional Porous MoS2-Reduced Graphene Oxide Film for High-performance Lithium-Ion Batteries

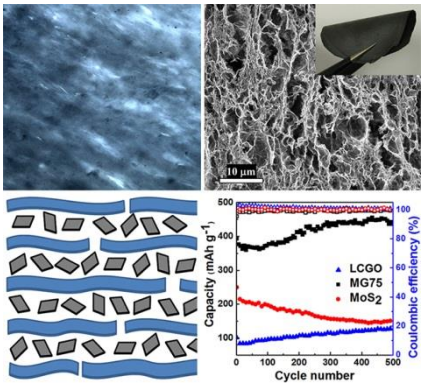

WILEY-VCH

ADVANCED FUNCTIONAL MATERIALS

Supporting Information

for Adv. Funct. Mater., DOI: 10.1002/adfm. 201700234

Self-assembly of Flexible Free-standing Three-Dimensional Porous MoS_2-Reduced Graphene Oxide Structure for High-performance Lithium-Ion Batteries

Yunfeng Chao, Rouhollah Jalili, Yu Ge, Caiyun Wang*, Tian Zheng, Kewei Shu, Gordon G. Wallace*

Supporting Information

Self-assembly of Flexible Free-standing Three-Dimensional Porous MoS_2-Reduced Graphene Oxide Structure for High-performance Lithium-Ion Batteries

Yunfeng Chao, Rouhollah Jalili, Yu Ge, Caiyun Wang*, Tian Zheng, Kewei Shu, Gordon G. Wallace*

ARC Centre of Excellence for Electromaterials Science, Intelligent Polymer Research Institute, AIIM Facility, Innovation Campus, University of Wollongong, NSW 2522, Australia.

E-mail: caiyun@uow.edu.au (C. W.), gwallace@uow.edu.au (G. G. W.)

Figure S1. LCGO dispersion (left) and MoS_2 dispersion (right) after heating at 70 ℃ overnight.

Equation S1. The equation to calculate the critical theoretical concentration (Φ) of 2D platelets for the transition between isotropic to nematic phase.[1]

$$\Phi = \frac{3}{8}\sqrt{3}\frac{t}{D}\frac{1+\sigma^2}{1+3\sigma^2}\rho D^3 \quad (1)$$

D^3 is a dimensionless number density for the isotropic to biphasic and subsequently biphasic to nematic transition concentrations; t, D, σ and ρ are sheet thickness, average GO lateral size, polydispersity and density, respectively.

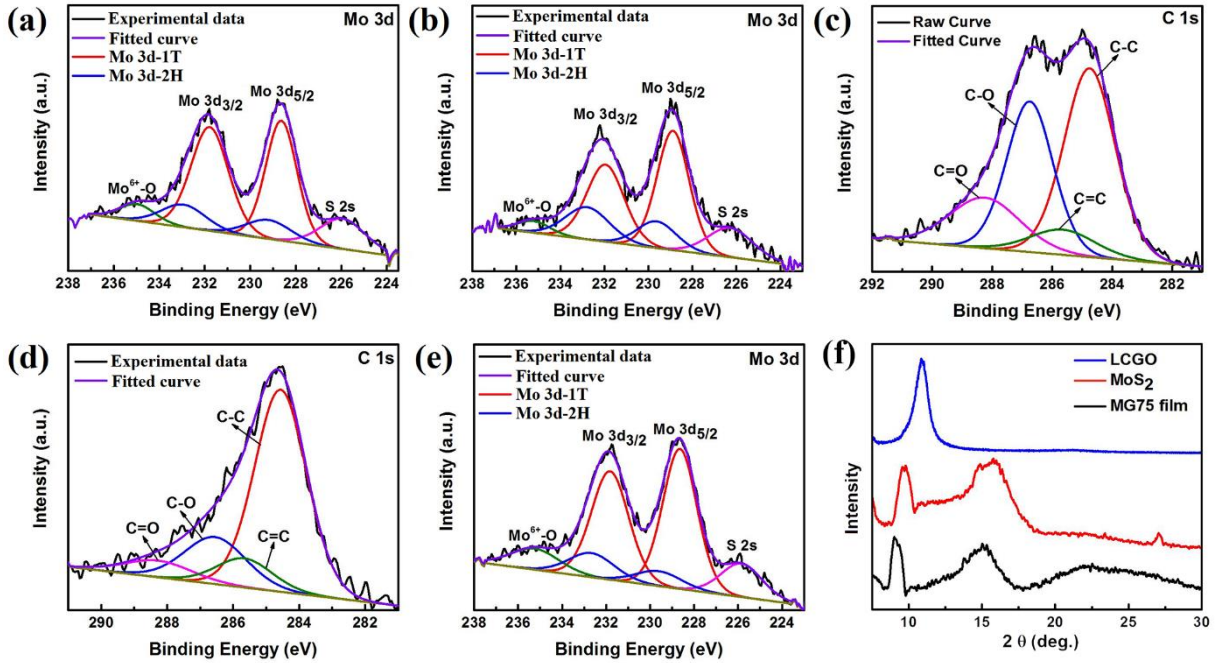

Figure S2. Mo3d XPS spectra of MoS_2 (a) and MG50 (b) films; C1s (c) XPS spectrum of LCGO film prepared by filtering LCGO dispersion; C1s (d) and Mo3d (e) XPS spectra of MG75 aerogel prepared by standing in ambient atmosphere for half a month; (f) XRD spectra of LCGO, MoS_2 and MG75 films.

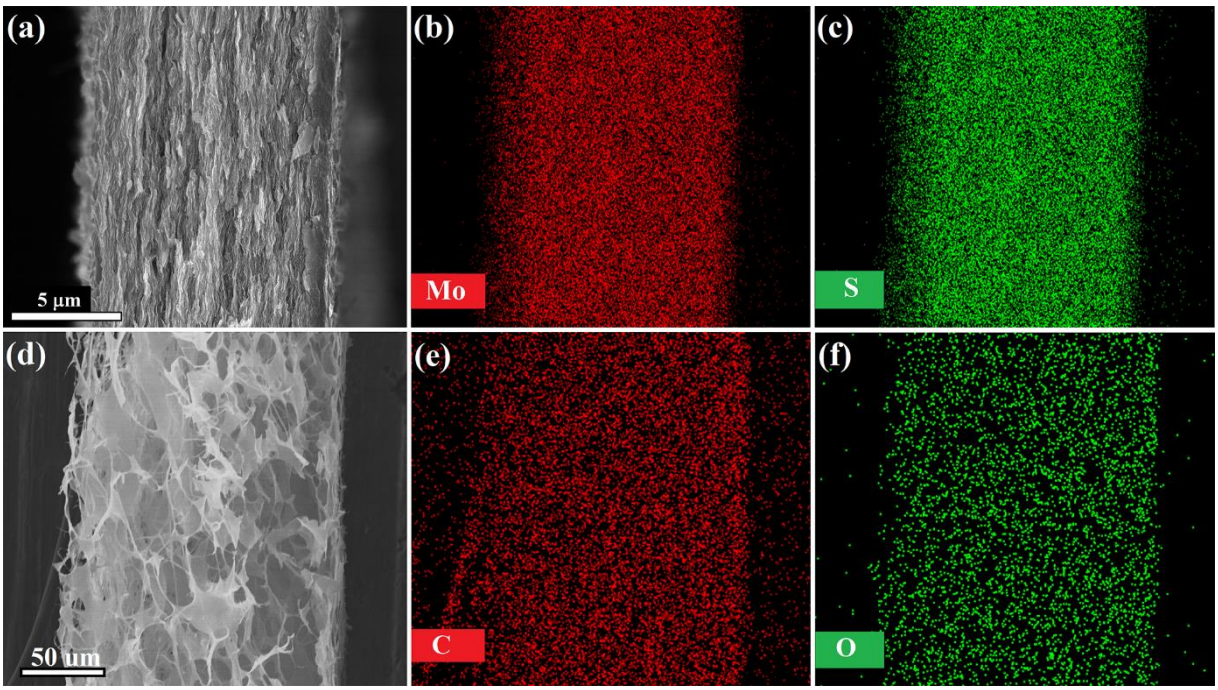

Figure S3. Cross-sectional SEM images and element mapping images of MoS_2 film (a-c) and LCGO film (d-f).

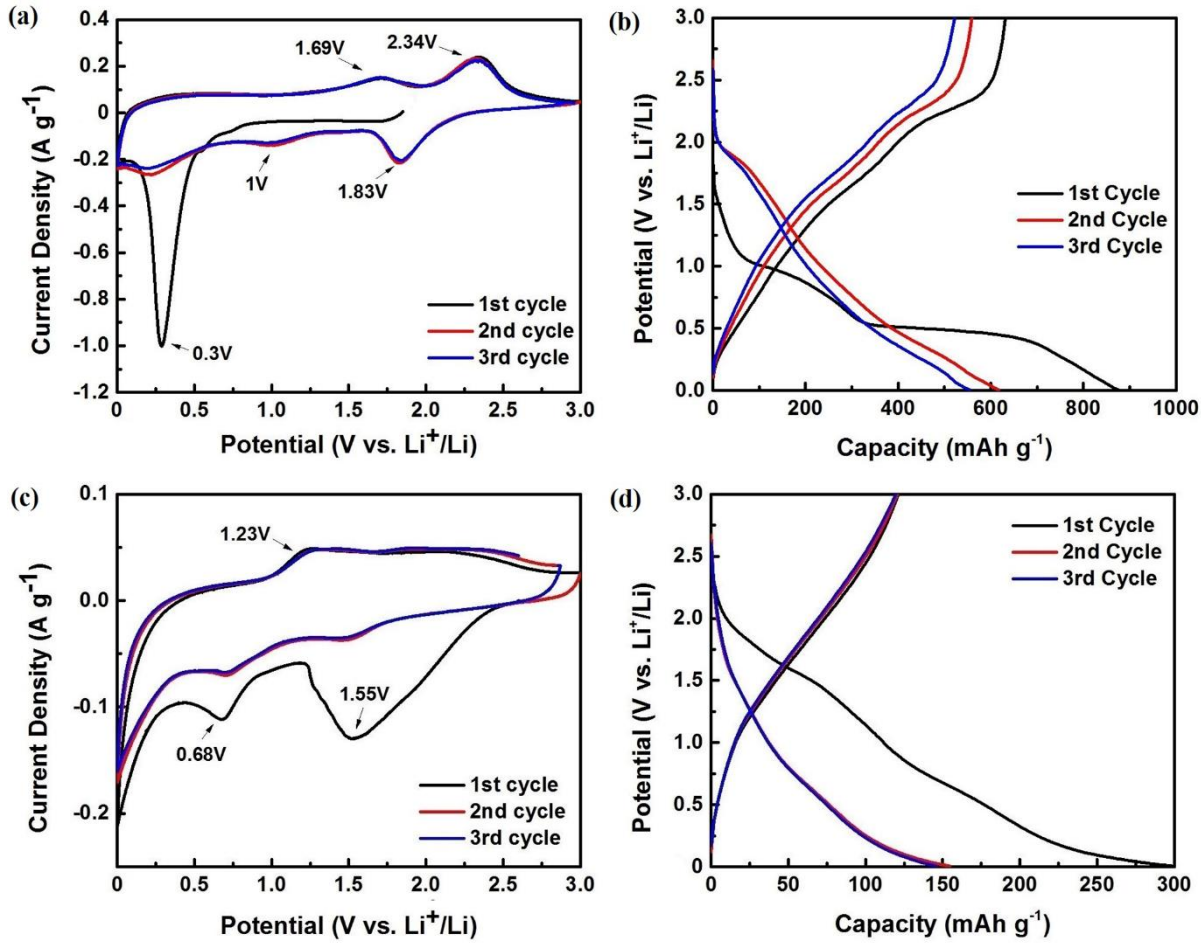

Figure S4. The first three cyclic voltammetry curves of MoS_2 film (a) and LCGO film (b) at a scan rate of 0.2 mV s^{-1}; The first three charge/discharge curves of LCGO film (c) at a current density of 100 mA g^{-1} over a potential range of 0.005 to 3 V.

Table S1. Cycling stability of MG75 film prepared in this study in comparison with the reported results for MG composites

Production	Cycling performance			Ref.
	Retention ratio (%)	Cycle number	Current density/A g^{-1}	
MG75 film	112.5	500	0.4	This work
MoS_2/Graphene paper	91.1	100	0.1	[2]
Honeycomb-like MoS_2@Graphene foam	85.8	60	0.2	[3]
Few-layer MoS_2-anchored graphene paper	101.1	700	0.5	[4]
Free-standing MoS_2/graphene hybrid film	94.2	500	0.5	[5]
N-doped graphene-MoS_2 film	96	200	0.1	[6]
MoS_2/graphene nanocomposite	91.1	200	0.1	[7]
MoS_2@graphene foam/CNT hybrid films	81.3	120	0.2	[8]
MoS_2-Graphene hybrid nanosheets	99	200	0.2	[9]
MoS_2/graphene composite	78	80	0.1	[10]
MoS_2/rGO composites	96.3	250	1	[11]
Few-Layered MoS_2/S-doped Graphene	92.6	300	0.1	[12]
Nanotile-likeMoS_2/Graphene hybrid	91.6	220	0.1	[13]

References:

[1] (a) R. Jalili, S. H. Aboutalebi, D. Esrafilzadeh, R. L. Shepherd, J. Chen, S. Aminorroaya Yamini, K. Konstantinov, A. I. Minett, J. M. Razal, G. G. Wallace, *Adv. Funct. Mater.* 2013, 23, 5345. (b) R. Jalili, S. Aminorroaya-Yamini, T. M. Benedetti, S. H. Aboutalebi, Y. Chao, G. G. Wallace, D. L. Officer, *Nanoscale* 2016, 8, 16862.

[2] M. Yang, S. Ko, J. S. Im, B. G. Choi, *J. Power Sources* **2015**, *288*, 76.

[3] J. Wang, J. Liu, D. Chao, J. Yan, J. Lin, Z. X. Shen, *Adv. Mater.* **2014**, *26*, 7162.

[4] Q. Liu, J. Huo, Z. Ma, Z. Wu, S. Wang, *Electrochim. Acta*, **2016**, *206*, 52.

[5] L. David, R. Bhandavat, G. Singh, *ACS nano* **2014**, *8*, 1759.

[6] T. Shan, S. Xin, Y. You, H. Cong, S. Yu, A. Manthiram, *Angew. Chem. Int. Ed.* **2016**, *55*, 1.

[7] A. Ambrosi, Z. Sofer, M. Pumera, *Small* **2015**, *11*, 605.

[8] J. Wang, J. Liu, J. Luo, P. Liang, D. Chao, L. Lai, J. Lin, Z. Shen. *J. Mater. Chem. A* **2015**, *3*, 17534.

[9] X. Zhang, Q. Zhang, Y. Sun, P. Zhang, X. Gao, W. Zhang, J. Guo. *Electrochim. Acta* **2016**, *189*, 224.

[10] G. Yuan, G. Wang, H. Wang, J. Bai. *J. Alloys and Compd.* **2016**, *660*, 62.

[11] D. H. Youn, C. Jo, J. Y. Kim, J. Lee, J. S. Lee. *J. Power Sources* **2015**, *295*, 228.

[12] X. Wang, G. Li, M. H. Seo, F. M. Hassan, M. A. Hoque, Z. Chen. *Adv. Energy Mater.* **2015**, 1501106.

[13] L. Ma, J. Ye, W. Chen, D. Chen, J. Lee. *Nano Energy* **2014**, *10*, 144.